von Neumann spin measurements with Rashba fields



2014 New J. Phys. 16 015013

(http://iopscience.iop.org/1367-2630/16/1/015013)

New Journal of Physics
The open access journal at the forefront of physics
Deutsche Physikalische Gesellschaft DPG | IOP Institute of Physics

# von Neumann spin measurements with Rashba fields

**E Ya Sherman**[1,2,3] **and D Sokolovski**[1,2]

[1] Departmento de Química-Física, Universidad del País Vasco, UPV/EHU, E-48080 Leioa, Spain
[2] IKERBASQUE Basque Foundation for Science, Bilbao, Spain
E-mail: evgeny.sherman@ehu.es

Received 30 May 2013, revised 23 November 2013
Accepted for publication 26 November 2013
Published 10 January 2014

*New Journal of Physics* **16** (2014) 015013

doi:10.1088/1367-2630/16/1/015013

**Abstract**

We show that dynamics in the spin–orbit coupling field simulate the von Neumann measurement of a particle spin. We demonstrate how the measurement influences the spin and coordinate evolution of a particle by comparing two examples of such a procedure. The first example is a simultaneous measurement of spin components, $\sigma_x$ and $\sigma_y$, corresponding to non-commuting operators, which cannot be accurately obtained together at a given time instant due to the Heisenberg uncertainty ratio. By mapping spin dynamics onto a spatial walk, such a procedure determines measurement-time averages of $\sigma_x$ and $\sigma_y$, which can already be precisely evaluated in a single short-time measurement. The other, qualitatively different, example is the spin of a one-dimensional particle in a magnetic field. Here, the measurement outcome depends on the angle between the spin–orbit coupling and magnetic fields. These results can be applied to studies of spin–orbit coupled cold atoms and electrons in solids.

## 1. Introduction: the spin–orbit coupling Hamiltonian and von Neumann measurement

Unusual properties [1–5], simplicity and ability to manipulate strength [6] put spin–orbit coupling in the focus of many research fields, where the mutual dependence of spin and

[3] Author to whom any correspondence should be addressed.

coordinate motion is important[4] [7]. For several decades, solids and solid-state structures were the systems to study the effects of spin–orbit coupling for electrons [8] and holes [9]. Recently, at least two completely new classes of systems with spin–orbit coupling were discovered and became new research fields. The first class is cold atoms in highly coherent laser fields [10–16]. For both types of particles, bosons and fermions, in addition to the spin–orbit coupling, an effective magnetic field can be produced optically. Studies of spin–orbit coupled cold atoms are related to the properties of new phases (see e.g. [17–19]) and macroscopic spin dynamics [20–22]. The other class is topological insulators [23], considered as promising elements for spintronics applications.

The very general character of spin–orbit coupling should have consequences for the fundamental quantum mechanics of single particles and their ensembles, and stimulate the search for these consequences in an experimentally realizable system. Motivated by the interest in the observability of the effects of spin–orbit coupling on the basic quantum mechanical level, here we show how it is directly related to the quantum measurement of spin-1/2 in terms of the procedure proposed by von Neumann. We begin with a general Hamiltonian (assume $\hbar \equiv 1$) of spin–orbit coupling linear in the two-dimensional particle momentum

$$\hat{H} = \hat{H}_0 + \hat{H}_{\rm so} + \hat{H}_{\rm Z}, \tag{1}$$

$$\hat{H}_0 = \frac{k_x^2 + k_y^2}{2M}, \tag{2}$$

$$\hat{H}_{\rm so} = \alpha(t)[\nu_x k_x\,(\mathbf{h_x}\cdot\boldsymbol{\sigma}) + \nu_y k_y(\mathbf{h_y}\cdot\boldsymbol{\sigma})], \quad \hat{H}_{\rm Z} = \frac{\Delta}{2}\,(\mathbf{b}\cdot\boldsymbol{\sigma})\,, \tag{3}$$

where $\hat{k}_x = -\mathrm{i}\partial/\partial x - \mathcal{A}_x$ and $\hat{k}_y = -\mathrm{i}\partial/\partial y - \mathcal{A}_y$ with corresponding components of gauge potential $\mathcal{A}_{x,y}$, $M$ is the effective mass and $\boldsymbol{\sigma}$ is the Pauli matrices pseudovector. Here, $\alpha(t)$ is the spin–orbit coupling parameter, in general time-dependent, $\boldsymbol{\nu}$ is a two-dimensional vector of unit length, $\mathbf{h_x}$ and $\mathbf{h_y}$ are the unit vectors corresponding to the type of spin–orbit coupling, $\Delta$ is the Zeeman splitting and $\mathbf{b}$ is the unit vector of the direction of the magnetic field. The conventional Rashba coupling is given by $\boldsymbol{\nu} = (1, 1)/\sqrt{2}$, $\mathbf{h_x} = \mathbf{y}$, $\mathbf{h_y} = -\mathbf{x}$, while the Dresselhaus couping is given by $\boldsymbol{\nu} = (1, 1)/\sqrt{2}$, $\mathbf{h_x} = \mathbf{x}$, and $\mathbf{h_y} = -\mathbf{y}$ ($\mathbf{x}$ and $\mathbf{y}$ are the corresponding coordinate system vectors). The value of $\alpha$ is in the range from 1–10 cm s$^{-1}$ for cold atoms to $10^6$ cm s$^{-1}$ for electrons in semiconductor nanostructures and $10^7$–$10^8$ cm s$^{-1}$ for topological insulators, where the kinetic energy vanishes [23], and surfaces with extremely strong spin–orbit coupling [24–27].

As a result, even at $\Delta = 0$, spin rotates around the axis in a direction which depends on $\mathbf{k}$. The operator of the particle's velocity depends on the orientation of the particle's spin,

$$\hat{v}_x = \mathrm{i}\,[H, x] = \frac{k_x}{M} + \alpha(t)\nu_x\,(\mathbf{h_x}\cdot\boldsymbol{\sigma})\,, \quad \hat{v}_y = \mathrm{i}[H, y] = \frac{k_y}{M} + \alpha(t)\nu_y(\mathbf{h_y}\cdot\boldsymbol{\sigma}). \tag{4}$$

The velocity components do not commute with each other even in the absence of an external gaugefield if the cross product of $\mathbf{h_x}$ and $\mathbf{h_y}$ is not zero. Even if it is zero, but $\mathbf{h_x}$, $\mathbf{h_y}$ and $\mathbf{b}$ are not collinear, the velocity components do not commute with the total Hamiltonian, strongly complicating the orbital dynamics.

Now we can see a connection between the Hamiltonian (1) and a quantum spin measurement. Consider a quantum system characterized by a multicomponent operator $(\hat{O}_x, \hat{O}_y, \hat{O}_z)$

[4] For interesting manifestations of this mutual influence, see [7].

coupled to the momentum $\hat{\mathbf{P}}$ of another system, or 'pointer', as $\sum \kappa_{ji} \hat{P}_j \hat{O}_i$, where $\kappa_{ji}$ is the corresponding coupling strength. This coupling is presented as $(-\mathrm{i}\partial/\partial X_j)\hat{O}_i$, where $\hat{\mathbf{X}}$ is the pointer position, and the Hamiltonian for the free pointer is $H_{\mathrm{pnt}}(\hat{\mathbf{P}}, \hat{\mathbf{X}})$. This coupling causes evolution of the quantities, characterized by the operator $\hat{\mathbf{O}}$ and, at the same time, makes the corresponding dynamics visible by mapping them on the pointer position in the coordinate space. Thus, by tracing the pointer position, one can expect to trace the motion of the operator components of $\hat{O}_i$. In the case of spin–orbit coupling, $\hat{\mathbf{P}}$ is the particle momentum and $\hat{\mathbf{O}}$ represents the spin components, as can be seen from equations (1)–(3). This simple observation, being the idea behind the von Neumann measurement, can have interesting consequences, including entanglement of the spin and coordinate degrees of freedom and, correspondingly, a spin dephasing in the measurement procedure, for experimentally realizable systems. We will describe these effects in this paper. Moreover, we will demonstrate that the dynamics of the pointer due to the Hamiltonian $H_{\mathrm{pnt}}(\hat{\mathbf{P}}, \hat{\mathbf{X}})$, e.g. its kinetic energy, influence the measurement procedure and its accuracy. This approach corresponds to the measurements by solving dynamical models, with some of them recently reviewed in [28].

To perform a spin measurement, we choose the spin–orbit coupling $\alpha(t)$ switched on for a finite time interval

$$\alpha(t) = \alpha \times \begin{cases} 1, & 0 \leqslant t \leqslant T, \\ 0, & t < 0, \quad t > T \end{cases} \tag{5}$$

making the Hamiltonian time-independent during the measurement. As a result, in the measurement procedure, the evolution of the initial state $\mathbf{\Psi}(\mathbf{r}|0)$, where $\mathbf{r}$ is the position and $\mathbf{\Psi}(\mathbf{r}|t)$ is the two-component spinor wave function, is given by

$$\mathbf{\Psi}(\mathbf{r}|t) = \exp(-\mathrm{i}\hat{H}t)\mathbf{\Psi}(\mathbf{r}|0). \tag{6}$$

For a translationally invariant system of our interest, it is convenient to represent equation (6) in the form

$$\mathbf{\Psi}(\mathbf{r}|t) = \int \mathbf{G}(\mathbf{r}-\mathbf{r}'|t)\mathbf{\Psi}(\mathbf{r}'|0)\,\mathrm{d}^D r' = \int \mathbf{G}\,(\mathbf{k}|t)\;\mathbf{\Psi}(\mathbf{k}|0)\,\mathrm{e}^{\mathrm{i}(\mathbf{k}\cdot\mathbf{r})}\frac{\mathrm{d}^D k}{(2\pi)^D}. \tag{7}$$

Here, $D$ is the system dimensionality, $\mathbf{G}\,(\mathbf{r}-\mathbf{r}'|t)$ is the $2\times 2$ Green function for the total Hamiltonian in equation (1) (e.g. see [29]), and $\mathbf{G}\,(\mathbf{k}|t)$ and $\mathbf{\Psi}(\mathbf{k}|0)$ are the corresponding Fourier components. During the measurement time $T$, the von Neumann pointer, that is the coordinate of the particle, provides information about the motion of its spin components. Here, the mapping onto the coordinate motion makes visible otherwise hidden spin dynamics over all possible Feynman paths in the spin subspace.

The rest of the paper is organized as follows. In section 2, we study a simultaneous measurement of non-commuting spin components for a two-dimensional particle with the Rashba spin–orbit coupling and analyse possible experimental realizations of the von Neumann spin measurement. We will show why the attempt of instantaneous measurement fails, and that the actual measured quantities are the average over the measurement time spin components. In section 3, we study the von Neumann measurement and measurement-induced dephasing of a spin rotating in a magnetic field for a one-dimensional particle with non-commuting spin–orbit and Zeeman terms. In section 4, we summarize the results and show a possible extension and generalizations of the relation between spin–orbit coupling and spin measurement procedures.

## 2. Measurement of two non-commuting spin components

### *2.1. Measurement, Feynman paths and outcome*

The Heisenberg uncertainty relation established the limit on precision of instantaneous measurement of observables corresponding to two non-commuting operators in terms of the expectation value of their commutator. Although this general statement is one of the basic properties of quantum motion, the measurement procedure itself is still an unresolved issue [30–35], even for momentum and coordinate observables. Arthurs and Kelly [30] considered two meters employed to jointly measure particle position and momentum. The analogue of the Arthurs–Kelly experiment for non-commuting spin components was proposed in [32]. An implementation of such a measurement through coupling to radiation modes was considered in [34], and through the coupling of quantum spin to classical Ising states in [35]. However, the straightforward interpretation of the proposed experiments is hardly possible. In this section we provide a recap of the measurement scheme using spin–orbit coupling [36], where coordinate pointers are attached to non-commuting spin components. For this purpose we return to the Hamiltonian (1) and study the spin dynamics of a single wave packet in the absence of an external magnetic field.

Without loss of generality, we choose the spin–orbit coupling in the conventional Rashba form. Neglecting the internal dynamics of the pointer (the exact condition will be given further in the text) we obtain the Schrödinger equation

$$\mathrm{i}\partial_t \mathbf{\Psi}(x, y|t) = -\mathrm{i}\widetilde{\alpha}(\partial_x\sigma_y - \partial_y\sigma_x)\mathbf{\Psi}(x, y|t), \tag{8}$$

with an initial condition

$$\mathbf{\Psi}(x, y|0) = \psi_0(x, y)\boldsymbol{\xi}, \tag{9}$$

where $\mathbf{\Psi}(x, y|t)$ and $\boldsymbol{\xi}$ are two-component spinors (we will usually employ the representation of $\sigma_z-$ eigenstates), $\psi_0(x, y)$ is the initial wave packet, and $\widetilde{\alpha} \equiv \alpha/\sqrt{2}$. Equation (8) describes spin-1/2 coupled to two von Neumann pointers [37] with positions $x$ and $y$, respectively, in an attempt to measure spin components $\sigma_y$ and $\sigma_x$ simultaneously.

Considering the first measurement of a single spin component, $\sigma_y$, by choosing for a moment $H_{\mathrm{so}} = -\mathrm{i}\widetilde{\alpha}\partial_x\sigma_y$, offers a useful insight. First, we present the initial state as $\mathbf{\Psi}(x, y|0) = \psi_0(x, y)(\zeta_1|1\rangle_y + \zeta_2|-1\rangle_y)$, where $|1\rangle_y$ and $|-1\rangle_y$ are the eigenstates of $\sigma_y$ with the corresponding eigenvalues. The operator $\exp(-\widetilde{\alpha}t\partial_x\sigma_y)$ splits this initial state into two components traveling along the $x$-axis with opposite speeds $\widetilde{\alpha}$ as $\zeta_1\psi_0(x - \widetilde{\alpha}t, y)|1\rangle_y + \zeta_2\psi_0(x + \widetilde{\alpha}t, y)|-1\rangle_y$. If the wave packets are well separated and the particle is found at a location $x$, $x/\widetilde{\alpha}t$ approximates the value of $\sigma_y = \pm 1$. The accuracy of the approximation depends on the width of the $\psi_0(x, y)$—for a very narrow initial distribution we would only have $x \approx \widetilde{\alpha}t$ or $x \approx -\widetilde{\alpha}t$, realizing a conventional von Neumann measurement of a single spin component.

However, our case is more complicated. Since $\sigma_x$ and $\sigma_y$, and, thus, $v_y$ and $v_x$, do not commute, the pointer in equation (8) does not have a well-defined two-component velocity. To study its motion, we slice the time interval $[0, T]$ into $L$ sub-intervals $\epsilon = T/L$, and take the limit by the Lie–Trotter formula [38]

$$\exp[-\widetilde{\alpha}T(\partial_x\sigma_y - \partial_y\sigma_x)] = \lim_{L\to\infty}[\exp(-\widetilde{\alpha}\epsilon\partial_x\sigma_y)\exp(\widetilde{\alpha}\epsilon\partial_y\sigma_x)]^L, \tag{10}$$

where

$$\exp(\pm\widetilde{\alpha}\epsilon\partial_j\sigma_i) = \sum_{m=\pm1}|m\rangle_i \exp\ (\pm m\widetilde{\alpha}\epsilon\partial_j)_i\langle m| \tag{11}$$

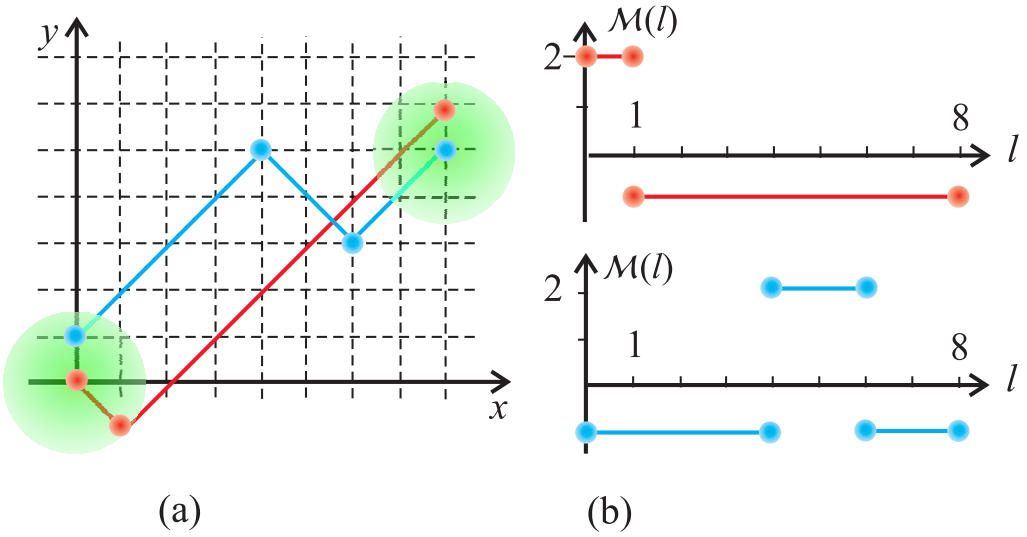


**Figure 1.** (a) Feynman paths for two possible virtual histories of the particles in the $xy$-plane ($L = 8$). Both the initial and final positions are unresolved, being located under the Gaussian (green circles) of width $w$. We consider a short measurement, where $w$ remains constant for $t < T$. (b) The time dependence of $\mathcal{M}(l)$ function in equations (14) and (15) for these two paths. For both paths $\langle\sigma_y\rangle_T = 1$. For the upper path $\langle\sigma_x\rangle_T = -3/4$ and for the lower path $\langle\sigma_x\rangle_T = -1/2$.

with $\sigma_i|m\rangle_i = m|m\rangle_i$ and $i = x, y$, corresponding to all possible, hidden in the absence of spin–orbit coupling, virtual Feynman walks on an infinite lattice $x(j_x) = j_x\widetilde{\alpha}\epsilon$, $y(j_y) = j_y\widetilde{\alpha}\epsilon$, $j_x, j_y = \ldots -1, 0, 1, \ldots$ reminiscent of Feynman's checkerboard for a Dirac electron [39]. In every time step the particle moves forwards or backwards along the $x$- and $y$-axis, and its position at the end of the measurement, $t = T$, is determined by the differences, $\Delta n_x$ and $\Delta n_y$, between the numbers of forward and backward steps taken in each direction or, more precisely, by the interference between all paths sharing the same $\Delta n_x$, and $\Delta n_y$ (see figure 1(a)). Next, we assign values $m_i(l) = \pm 1$, $l = 1, \ldots, L$ to $\sigma_i$ in each step and define

$$\Delta n_i = \sum_{l=1}^{L} m_i(l). \tag{12}$$

As a result, finding the pointer at a location $(x, y)$ determines the *time averages* of the spin components, $\langle\sigma_x\rangle_T$ and $\langle\sigma_y\rangle_T$, defined for the spin-space Feynman paths (figure 1(b)) as

$$\langle\sigma_i\rangle_T \equiv \frac{1}{T}\int_0^T \sigma_i(t)\,\mathrm{d}t \tag{13}$$

to an accuracy determined by the position spread of the initial $\psi_0(x, y)$. In this figure, we characterize both spins by a single function

$$\mathcal{M}(l) = 2, \quad \text{if} \quad m_x(l) = m_y(l) = 1, \quad \mathcal{M}(l) = 1, \quad \text{if} \quad m_x(l) = 1, \quad m_y(l) = -1, \tag{14}$$

$$\mathcal{M}(l) = -1, \quad \text{if} \quad m_x(l) = -1, \quad m_y(l) = 1, \quad \mathcal{M}(l) = -2, \quad \text{if} \quad m_x(l) = m_y(l) = -1. \tag{15}$$

The inverse is given by: $m_x(l) = \operatorname{sign}\mathcal{M}(l)$, and $m_y(l) = (-1)^{\mathcal{M}}(l)\operatorname{sign}\mathcal{M}(l)$.

### *2.2. Transition amplitudes and expectation values of observables*

To study the details of the measurement procedure, we begin by introducing the radius $R_{so} \equiv \widetilde{\alpha} T$ and note that a particle initially localized at the origin would never leave the 'allowed' circle $r \equiv (x^2 + y^2)^{1/2} \leqslant R_{so}$. To study the coupled evolution, we define the initial state as the spatial Gaussian, corresponding to the particle release from the ground state of a harmonic potential

$$\mathbf{\Psi}(x, y|0) = \frac{\sqrt{2}}{\sqrt{\pi} w} \exp\ (-r^2/w^2) \begin{bmatrix} \xi_1 \\ \xi_2 \end{bmatrix}, \tag{16}$$

and the matrix $\mathbf{U}(x, y|T; \psi_0)$, such that at the end of the measurement (in the following we omit the explicit dependence on the initial state $\psi_0(x, y)$):

$$\mathbf{\Psi}(x, y|T) = \mathbf{U}(x, y|T) \begin{bmatrix} \xi_1 \\ \xi_2 \end{bmatrix}. \tag{17}$$

Using equations (6) and (7) for the Hamiltonian corresponding to equation (8), we find that in the cylindrical coordinates $\mathbf{U}(r, \varphi|T)$ is a Hermitian matrix with

$$U_{11}(r|T) = U_{22}(r|T) = w \int_0^\infty \exp(-k^2 w^2/4) \cos\,(R_{so} k)\ J_0(kr) \frac{k\mathrm{d}k}{\sqrt{2\pi}}, \tag{18}$$

$$U_{12}(r, \varphi|T) = U_{21}{}^*(r, \varphi|T) = \mathrm{i} e^{-\mathrm{i}\varphi} w \int_0^\infty \exp(-k^2 w^2/4) \sin\,(R_{so} k)\ J_1\,(kr)\ \frac{k\mathrm{d}k}{\sqrt{2\pi}}, \tag{19}$$

where $J_n(z)$ is the Bessel function of the first kind of order $n$, and $\varphi$ is the angle between $\mathbf{r}$ and the $x$-axis[5] [40]. As a result, the initial state shows a two-dimensional spread and after the measurement produces the density $\mathbf{\Psi}^\dagger(r, \varphi|T)\mathbf{\Psi}(r, \varphi|T) = |\Psi_1^2(r, \varphi|T)| + |\Psi_2^2(r, \varphi|T)|$, concentrated in a ring of a radius $R_{so}$, width $\approx w$ and dependent on the angle $\varphi$. The large argument asymptotes of the Bessel functions [41]

$$J_n(kr) \sim \sqrt{\frac{2}{\pi kr}} \cos(kr - n\pi/2 - \pi/4) \tag{20}$$

show that in the limit $w \to 0$ the integrals become singular as $r$ approaches $R_{so}$, and the measurement is possible only with a finite accuracy at non-zero width.

It is worth mentioning that an additional obstacle to a highly accurate measurement appears due to a finite mass of the particle, where packet spreads with the characteristic speed of the order of $v_{sp} = 1/wM$. Thus, the conditions of the precise measurement can be formulated as: (i) $\alpha \gg v_{sp}$, to ensure that the wave packet dynamics are due to the spin–orbit coupling and not to the broadening resulting from the finite $M$; and (ii) $\alpha T \gg w$ to ensure that the split of the wave packet at time $T$ is sufficient to perform the measurement.

Three implementations of this procedure can be considered:

1. For electrons in semiconductor structures with typical $\alpha \sim 10^6\,\mathrm{cm\,s^{-1}}$, that is, in conventional units, $\hbar\alpha \sim 10\,\mathrm{meV\,nm}$, and $M \sim 5 \times 10^{-29}\,\mathrm{g}$, the condition $\alpha \gg v_{sp}$ can be achieved for $w > 100\,\mathrm{nm}$, and corresponding $T > 10^{-11}\,\mathrm{s}$.

[5] A similar approach was applied for the Green function in graphene by Inglot and Dugaev [40].

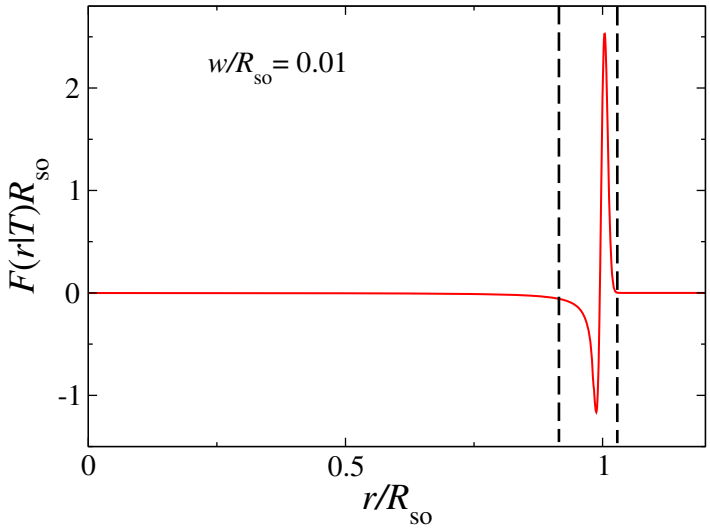


**Figure 2.** The radial function $F(r|T)$ for $w/R_{so} = 0.01$. Vertical dashed lines mark the interval (ring) containing most of the probability density.

2. For topological insulators, $\alpha \sim 10^8\,\mathrm{cm\,s^{-1}}$ ($\hbar\alpha \sim 1\,\mathrm{eVnm}$), with infinite $M$, and, therefore, the first condition $\alpha \gg v_{sp}$ is always satisfied. However, at the moment, it is difficult to prepare and control individual electron states in these systems.
3. For cold bosonic and fermionic atoms, taking $\alpha \sim 10\,\mathrm{cm\,s^{-1}}$ ($\hbar\alpha \sim 10^{-6}\,\mathrm{K}\,\mu\mathrm{m}$, with the relevant energy scale measured in Kelvins and the distance in microns) and fermion $^{40}$K as an example, we obtain $w > 10^{-4}\,\mathrm{cm}$ and $T > 10^{-5}\,\mathrm{s}$. We mention here that coherent many-particle spin–orbit coupled Bose–Einstein condensates with the pseudospin 1/2 such as $^{87}$Rb may be an interesting system for the proposed measurement. Condensates with a weak effective interatomic interaction are preferable for this purpose since, with the increase in this interaction, the wave packet spread may be controlled by the interatomic repulsion or attraction rather than by the initial width. As a result, the corresponding spreading rate should be taken in the above criteria of accurate measurement.

For a highly accurate measurement with $w \ll R_{so}$, the main contributions to the integrals in (18) and (19) come from the domain where $1/R_{so} \ll k \sim 1/w$. Replacing the Bessel functions by their asymptotes (20) and neglecting the contribution of rapidly oscillating ($\sim\cos(R_{so}k)$) terms in the integrand yields

$$\mathbf{U}(r, \varphi|T) \sim F(r|T)[\sigma_0 + \sigma_x \sin\varphi - \sigma_y \cos\varphi], \tag{21}$$

$$F(r|T) = \frac{w}{\sqrt{R_{so}}} \int_0^\infty \exp(-k^2w^2/4)\cos[(r - R_{so})k + \pi/4]k^{1/2}\frac{\mathrm{d}k}{2\pi}, \tag{22}$$

demonstrating that spin-coordinate entanglement is, in fact, spin-angle entanglement. For a small $w$, the radial function $F(r|T)$, obtained in [36], has a maximum and a minimum close to $r = R_{so}$, rapidly decreases for $r > R_{so}$, and exhibits a somewhat slower decay for $r < R_{so}$, as shown in figure 2. Figure 1 corresponds to a less accurate measurement, where $R_{so}$ and $w$ are of the same order of magnitude.

Although the probability density is concentrated in a narrow vicinity of $R_{so}$, the broad angular distribution in equation (21) appearing as a result of the measurement has a relatively

broad distribution of moments

$$\langle x(T)\rangle = -R_{\rm so}\langle\sigma_y(0)\rangle/2, \quad \langle y(T)\rangle = R_{\rm so}\langle\sigma_x(0)\rangle/2, \tag{23}$$

$$\langle x^2(T)\rangle = R_{\rm so}^2/2, \quad \langle y^2(T)\rangle = R_{\rm so}^2/2, \tag{24}$$

where $\langle\sigma_y(0)\rangle$ and $\langle\sigma_x(0)\rangle$ are expectation values of corresponding spin components at $t = 0$. The $\varphi$-dependent spin orientations at $t = T$ were presented in [36].

To conclude this section, switching a Rashba coupling for a particle moving on a plane over a short time $T$ simulates a von Neumann measurement of two non-commuting spin components. Here, the particle itself plays the role of a pointer which correlates its position, $(x, y)$, with the time average of the corresponding spin components, $\langle\sigma_x\rangle_T$ and $\langle\sigma_y\rangle_T$, evaluated along Feynman paths defined for the two spin variables (figure 1). There are infinitely many trajectories which share the same $\langle\sigma_x\rangle_T$ and $\langle\sigma_y\rangle_T$ and lead to the same pointer position. We stress here that since these time averages are not instantaneous values of the spin components, they can be measured simultaneously to any desired accuracy. Indeed, the Feynman paths shown in figure 1 have no intrinsic time scale and can be cut into arbitrarily small $\epsilon/T \to 0$ pieces. Thus, even in the pulse limit $T \to 0$, under condition $\widetilde{\alpha}T = \text{const}$ one does not attain unique instantaneous values of the two spin components: no matter how small $T$ is, all paths shown in figure 1(a) contribute to the transition amplitude (17), densely filling the area with $r \leqslant R_{\rm so}$, and no measurement can catch $\sigma_x$ and $\sigma_y$ simultaneously. Thus, the fact that the particle can choose an infinite set of completely different Feynman paths at any short measurement time prevents us from defining sharp instantaneous values for the non-commuting spin components.

## 3. Measurement of spin in a magnetic field

### *3.1. Measured quantity, Feynman paths and Green functions*

In this section, we consider the measurement of a spin of a particle in a one-dimensional system, where the velocity operator and the Zeeman term do not commute. Such a measurement can be realized in semiconductor quantum wires [42] and narrow wave guides for the Bose–Einstein condensates [43, 44] with implemented spin–orbit coupling. We take the one-dimensional version of the Hamiltonian (1) as

$$\hat{H}_{\rm 1D} = \frac{k^2}{2M} + \alpha k\sigma_z + \frac{\Delta}{2}(\mathbf{b}\cdot\boldsymbol{\sigma}) \tag{25}$$

and assume that at $t = 0$, $\boldsymbol{\Psi}(x|0) = \psi_0(x)\boldsymbol{\xi}$ and $\mathbf{b} = (\sin\theta, 0, \cos\theta)$. We neglect the diamagnetic effects of vector potential $\mathcal{A}_{x,y}$ in a one-dimensional system. In addition, we note that for cold atoms [10–16], a synthetic Zeeman-like coupling can be realized without diamagnetic terms. Here, the spin–orbit coupling term $\alpha k\sigma_z$ satisfies the condition of the von Neumann measurement and the resulting dynamics simulate the quantum measurement [45] of a single spin component, $\sigma_z$ in this case. Despite its apparent simplicity, this system demonstrates rather non-trivial behavior, presented below.

Although, unlike in the previous section, only one component is measured, the spin is not static, but undergoes a precession due to the Zeeman term in (25). With the spin–orbit coupling turned on, each component of the particle's momentum adds an additional field along the $z$-axis. As a result, the spin moves in a magnetic field, whose direction and magnitude are *fundamentally* uncertain. The velocity term $\alpha\sigma_z$ given by the commutator $\mathrm{i}[\hat{H}_{\rm 1D}, x]$, does not

commute with the Hamiltonian, and wave packet non-uniformly spreads even if the particle's mass is infinite. We begin with the general properties of these dynamics and then discuss the expectation values of observables in relation to the von Neumann measurement procedure.

Following the approach from the previous section, and neglecting for a moment the kinetic energy, we slice the interval $[0, T]$ into $L$ sub-intervals of a length $\epsilon$, apply the Lie–Trotter formula now to $\exp\{-\mathrm{i}\epsilon[\alpha\hat{k}\sigma_z + \Delta\,(\mathbf{b}\cdot\boldsymbol{\sigma})\,/2]\}$, and introduce virtual Feynman paths, where $\sigma_z$ takes a value $s_j = \pm 1$ at each $\epsilon$-interval, $j = 1, 2, \ldots L$. The exact propagator can be expressed as a path sum. Taking $L \to \infty$, we obtain

$$\exp(-\mathrm{i}\hat{H}_{1\mathrm{D}}T) = \sum_{\text{paths}} \hat{U}_{1\mathrm{D}}[\text{path}], \tag{26}$$

where the operator

$$\hat{U}_{1\mathrm{D}}[\text{path}] = \exp\left(-\alpha T\langle\sigma_z\rangle_T\partial_x\right)\lim_{L\to\infty}|s_L\rangle\langle s_L|\exp\left[-\mathrm{i}\epsilon\Delta\,(\mathbf{b}\cdot\boldsymbol{\sigma})\,/2\right]|s_{L-1}\rangle\ldots\langle s_2|$$
$$\times\exp\left[-\mathrm{i}\epsilon\Delta\,(\mathbf{b}\cdot\boldsymbol{\sigma})\,/2\right]|s_1\rangle\langle s_1|, \tag{27}$$

translates the initial state by a distance $\alpha\langle\sigma_z\rangle_T T$. If $\psi_0(x)$ is completely localized, $|\psi_0^2(x)| = \delta(x)$, from the final position of the pointer $x$ one can accurately deduce the value of $\langle\sigma_z\rangle_T = x/\alpha T$. A spread in the initial positions leads to a finite error in the determination of $\langle\sigma_z\rangle_T$. Finally, including the pointer kinetic energy leads to spreading of the initial wave packet $\psi_0(x)$ in the measurement time. The corresponding Feynman checkerboard in the $(t, x)$ space mapping spin motion on spatial dynamics is shown in figure 3(a).

Although the Lie–Trotter formula is valuable for the understanding of the virtual Feynman paths, equation (7) is more convenient for detailed calculations, similar to the approach used in section 2. Introducing notations $\gamma \equiv \Delta\cos\theta/\alpha$, $q \equiv 2k + \gamma$, $C \equiv \cos(t\sqrt{q^2\alpha^2 + \widetilde{\Delta}^2}/2)$ and $S \equiv \sin(t\sqrt{q^2\alpha^2 + \widetilde{\Delta}^2}/2)$, where $\widetilde{\Delta} \equiv \Delta\sin\theta$, and using equation (6) with the Hamiltonian (25), we obtain the Green function in equation (7) in the form

$$G_{11}(x|t) = \mathrm{e}^{-\mathrm{i}\gamma x/2}\int_{-\infty}^{\infty}\left[C - \mathrm{i}\frac{q\alpha}{\sqrt{q^2\alpha^2 + \widetilde{\Delta}^2}}S\right]\mathrm{e}^{\mathrm{i}qx/2}\,\mathrm{e}^{-\mathrm{i}(q/2-\gamma/2)^2t/2M}\frac{\mathrm{d}q}{4\pi}, \tag{28}$$

$$G_{22}(x|t) = \mathrm{e}^{-\mathrm{i}\gamma x/2}\int_{-\infty}^{\infty}\left[C + \mathrm{i}\frac{q\alpha}{\sqrt{q^2\alpha^2 + \widetilde{\Delta}^2}}S\right]\mathrm{e}^{\mathrm{i}qx/2}\,\mathrm{e}^{-\mathrm{i}(q/2-\gamma/2)^2t/2M}\frac{\mathrm{d}q}{4\pi}, \tag{29}$$

$$G_{12}(x|t) = G_{21}(x|t) = -i\mathrm{e}^{-\mathrm{i}\gamma x/2}\widetilde{\Delta}\int_{-\infty}^{\infty}\frac{S}{\sqrt{q^2\alpha^2 + \widetilde{\Delta}^2}}\mathrm{e}^{\mathrm{i}qx/2}\,\mathrm{e}^{-\mathrm{i}(q/2-\gamma/2)^2t/2M}\frac{\mathrm{d}q}{4\pi}. \tag{30}$$

We begin with two simple limiting cases, taking $v_{\mathrm{sp}} = 0$ for simplicity.

***Case 1.*** The spin–orbit coupling and Zeeman terms commute, with $\theta = 0$ as an example. The Green function

$$\mathbf{G}(x - x'|T) = \begin{bmatrix}\mathrm{e}^{-\mathrm{i}T\Delta/2}g_0(x - x' - \alpha T|T) & 0\\ 0 & \mathrm{e}^{\mathrm{i}T\Delta/2}g_0(x - x' + \alpha T|T)\end{bmatrix} \tag{31}$$

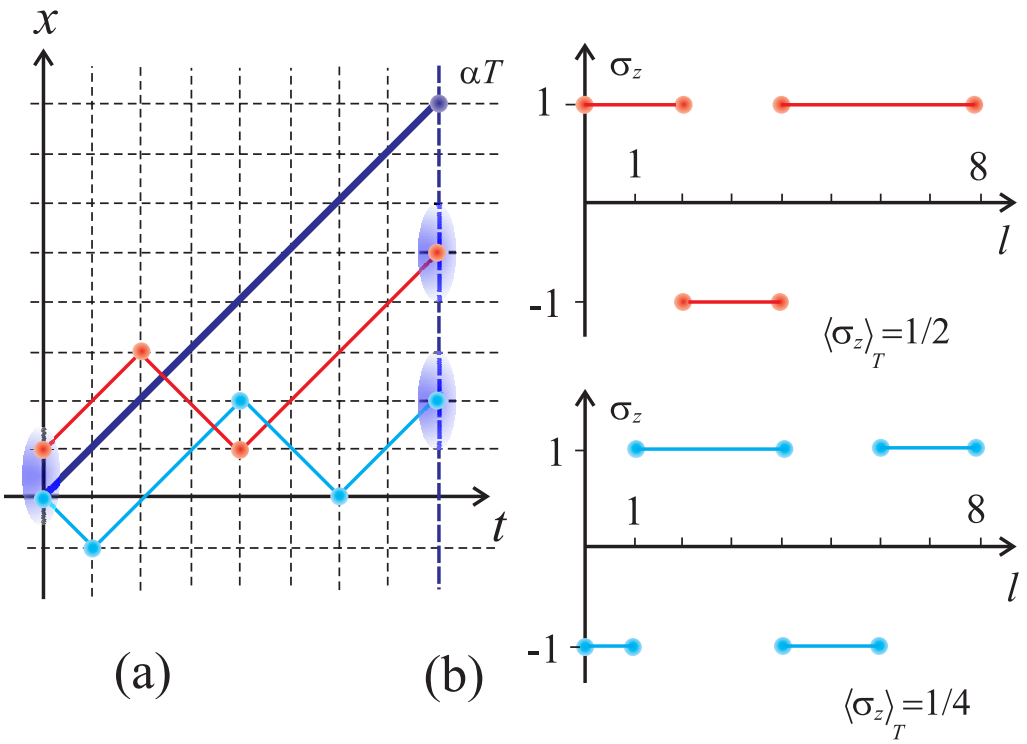


**Figure 3.** (a) Feynman checkerboard in the $(x|t)$ space for two possible virtual paths (we take $L = 8$). Initially unresolved positions under the one-dimensional Gaussian of the widths $w$ (shown as the elongated ellipses) become resolved at the end of the measurement at $t = T$. The bold straight line corresponds to one of the possible paths $x = \pm\alpha t$ in the absence of a magnetic field. (b) The time dependence of $\sigma_z$ corresponding to the particle displacement for these two paths.

is diagonal in the spin space. Here, $g_0(x|t) = (M/2\pi it)^{1/2}\exp(iMx^2/2t)$ is the free particle propagator[6] [39, 46], which in the limit of infinite $M$ tends to the Dirac $\delta(x)-$function. For a non-zero $\sin\theta$, the Green function (31) is valid for a short time $t \ll 1/\widetilde{\Delta}$, where the effect of the magnetic field on the spin precession is still weak.

***Case 2.*** Without spin–orbit coupling, $\alpha = 0$, the Green function factorizes into a free propagator in the coordinate space and a spin part describing Larmor precession

$$\mathbf{G}(x - x'|T) = \exp\left[-i\frac{\Delta}{2}(\mathbf{b}\cdot\boldsymbol{\sigma})T\right]g_0(x - x'|T). \tag{32}$$

No spin measurement can be done here: although all virtual Feynman paths in figure 3(b) are possible and interfere, they cannot be mapped on the $x$-coordinate motion.

In the general case of non-commuting spin–orbit and Zeeman terms, the particle can choose all the paths shown in figure 3(a), where $x(T) - x(0) = \alpha\langle\sigma_z\rangle_T$, the same as discussed for the two-dimensional motion. These dynamics are complicated due to spin precession in the magnetic field, leading to a non-zero sum of contributions from different paths. The precession

[6] Some useful recipes for Feynman path integrals were given in [46].

stops once a steady spin state with $\langle\sigma_y(\infty)\rangle = 0$ is reached, although the wave packet continues to move and to spread.

### *3.2. Finite time measurement and coupled spin-coordinate evolution*

To focus on the effect of spin–orbit coupling, we consider (if not explicitly stated otherwise) the particle of infinite mass, avoiding the packet broadening due to its initial finite width. The infinite mass condition is essentially the first requirement of a precise measurement, $\alpha \gg v_{\rm sp}$, formulated in section 2. To illustrate the origin of the complicated character of spin dynamics even in the infinite mass limit, we present the continuity equation

$$\frac{\partial\rho(x|t)}{\partial t} + \frac{\partial j(x|t)}{\partial x} = 0, \tag{33}$$

where $\rho(x|t) = \mathbf{\Psi}^\dagger(x|t)\mathbf{\Psi}(x|t)$ is the probability density, and $j(x|t) = \mathbf{\Psi}^\dagger(x|t)\sigma_z\mathbf{\Psi}(x|t)$ is the spin-determined flux. The resulting local velocity

$$v(x|t) = \frac{\mathbf{\Psi}^\dagger(x|t)\sigma_z\mathbf{\Psi}(x|t)}{\mathbf{\Psi}^\dagger(x|t)\mathbf{\Psi}(x|t)} \tag{34}$$

strongly varies with time and coordinates, leading in turn to the non-trivial dependence of probability and current densities.

We begin with the snapshots of the probability and spin densities showing the role of the width of the packet as the measurement tool. Although our approach is general, in calculations we use (as in section 2) the Gaussian initial wave function in the coordinate and momentum spaces

$$\psi_0(x) = \frac{1}{\sqrt[4]{\pi w^2}}\mathrm{e}^{-x^2/2w^2}, \quad \psi_0(k) = (2\sqrt{\pi}\,w)^{1/2}\mathrm{e}^{-k^2w^2/2} \tag{35}$$

and the initial spin state

$$\xi_1 = \cos(\beta/2)\ \mathrm{e}^{\mathrm{i}\phi}, \quad \xi_2 = \sin(\beta/2)\,. \tag{36}$$

We use equation (7) with the Hamiltonian (25) and corresponding Green functions (28)–(30) to obtain time and coordinate-dependent wave functions.

Figure 4 shows the distribution of density and velocity for dimensionless time $t = 2\pi$ and different packet widths. Figure 5 shows the effect of packet spread; that is, the internal evolution of the pointer due to the kinetic energy in the Hamiltonian. The spread of the pointer state decreases the accuracy of the measurement since it considerably decreases the available range of momenta. If the mass of the particle is infinite, the range of momenta is of the order of $1/w$. If the spread velocity $v_{\rm sp} = 1/wM$ is non-zero, at large $t$ the momentum spread decreases (see equations (28)–(30)) as $1/\sqrt{wv_{\rm sp}t}$, and, therefore, fine details of the Green function become gradually smeared and the spin measurement accuracy decreases with time, since the displacement of the particle is determined not only by the spin dynamics, but also by the wave packet's spreading. This statement can be understood with the following optical analogy. If $v_{\rm sp} = 0$, the Green function is seen through a magnifying glass with a given resolution, smearing its finer details. For non-zero $v_{\rm sp}$, the Green function is seen through a diffraction grating

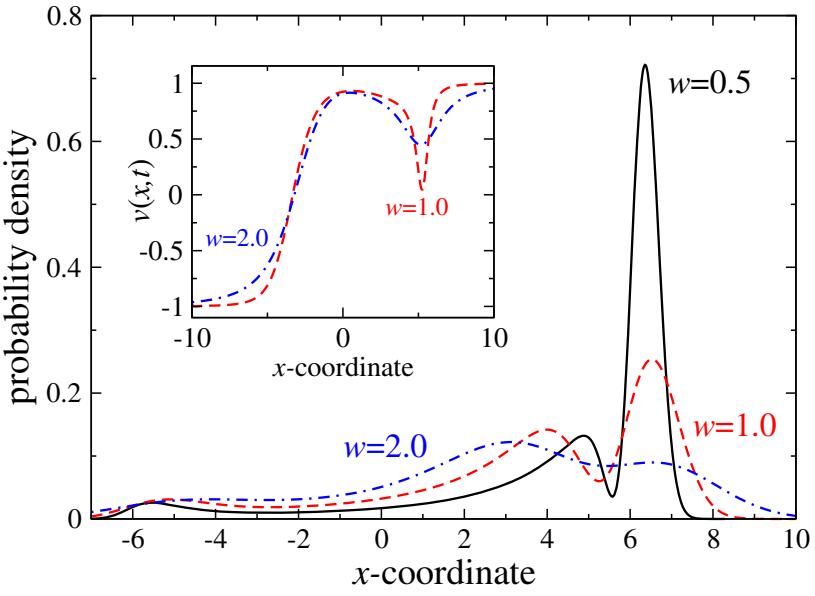


**Figure 4.** Total density as a function of the coordinate at $t = 2\pi$ for packet widths $w$ shown in the plot. The inset shows the coordinate distribution of velocity for $w = 1.0$ and 2.0. A similar dip at coordinate $r$ close to $R_{so}$, resulting from the interference of different paths, is seen in calculations for two-dimensional walks, as shown in figure 2 [36]. Here and in what follows, we use units $1/\widetilde{\Delta}$ for time, $\alpha/\widetilde{\Delta}$ for length, $\theta = \pi/4$ and $\xi_1 = 1$.

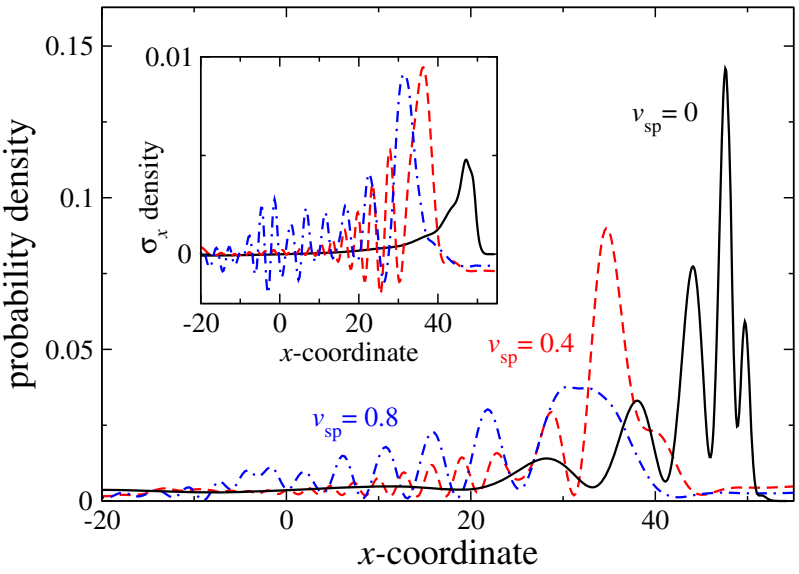


**Figure 5.** Total density as a function of the coordinate at $t = 16\pi$ and $w = 1$ for different $M$-dependent velocities of the initial state spread $v_{sp} = 0$, 0.4 and 0.8, as shown near the plots. The inset shows (with the corresponding style of the lines) the distribution of density of the $x$-component of spin $\mathbf{\Psi}^{\dagger}(x|t)\sigma_x\mathbf{\Psi}(x|t)$.

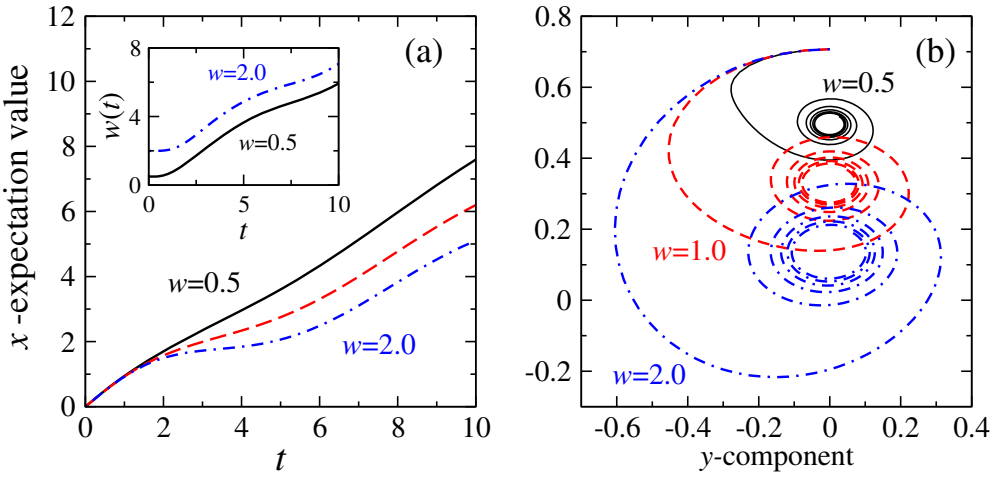


**Figure 6.** (a) Time dependence of the expectation value of the coordinate $\langle x(t)\rangle$ for different packet widths, shown near the plots. The inset shows fast broadening of the packet. (b) The $(\langle\sigma_y\rangle, \langle\sigma_\perp\rangle)$ trajectory. The dashed lines in (a) and (b) correspond to the same packet width.

with a relatively large period, which increases with time, smearing the details to an even greater extent.

To make a comparison with the analysis of the previous section, we calculate the expectation values of coordinate- and spin-related observables to see the relationship between them. We begin by tracing the following quantities:

$$\langle x(t)\rangle = \int_{-\infty}^{\infty} \mathbf{\Psi}^{\dagger}(x|t)x\mathbf{\Psi}(x|t)\,\mathrm{d}x, \tag{37}$$

$$w(t) = \sqrt{2}\sqrt{\langle x^2(t)\rangle - \langle x(t)\rangle^2} \tag{38}$$

for the expectation value of coordinate $\langle x(t)\rangle$ and width of the packet $w(t)$, respectively.

Figure 6(a) presents the expectation value $\langle x(t)\rangle$ for different initial widths of the packet and the time-dependent packet width in the inset. For any width at short times we obtain $\langle x(t)\rangle = \alpha t$, when all possible paths are in the vicinity of the straight line in figure 3(a). After some time, dependent on $w$, the spin explores other Feynman walks, and the dependence becomes asymptotically linear with the main term $\langle x(t)\rangle = \alpha\langle\sigma_z(\infty)\rangle t$. The inset shows the increase in the packet width with time, where different displacements $x - x' = \alpha t\langle\sigma_z\rangle_t \leqslant \alpha t$ are possible due to the spin precession in the magnetic field. The $x(t)$-dependences split here, and the packets start to broaden at dimensionless $t$ close to $\pi$, where the spin makes a half-turn. We emphasize that the packet broadening and nonlinear $\langle x(t)\rangle$-dependence are solely due to the non-commutativity of the Zeeman and the Rashba terms.

### *3.3. Spin decoherence and long measurement*

To better understand the coupled coordinate and spin dynamics, we consider the evolution of spin components by tracing the quantities

$$\langle\sigma_i(t)\rangle = \int_{-\infty}^{\infty} \mathbf{\Psi}^{\dagger}(x|t)\sigma_i\mathbf{\Psi}(x|t)\,\mathrm{d}x = \mathrm{tr}[\hat{\boldsymbol{\rho}}(t)\sigma_i] \tag{39}$$

calculated with the spin density matrix $\hat{\boldsymbol{\rho}}(t)$

$$\hat{\boldsymbol{\rho}}(t) = \int_{-\infty}^{\infty} \boldsymbol{\Psi}(x|t)\boldsymbol{\Psi}^{\dagger}(x|t)\,\mathrm{d}x. \tag{40}$$

With the increase in $t$, the different evolution of spinor components $\Psi_1(x|t)$ and $\Psi_2(x|t)$ produces a spin-coordinate entanglement and makes what was initially a pure spin state with $\mathrm{tr}\,\hat{\boldsymbol{\rho}}^2(0) = 1$ a mixed one with $\mathrm{tr}\,\hat{\boldsymbol{\rho}}^2(t) < 1$. As a result, the spin subsystem experiences a decoherence in the measurement process, and the spin moves from the initial position at the Bloch sphere $\sum_i \langle\sigma_i(0)\rangle^2 = 2\,\mathrm{tr}\,\hat{\boldsymbol{\rho}}^2(0) - 1$, to the inner part of the corresponding Bloch ball, where this sum is less than one. The spin-dependent velocity in a system with the Hamiltonian (25) determines the general relation between expectation values of spin and coordinate as $\langle v(t)\rangle \equiv \mathrm{d}\,\langle x(t)\rangle\,/\mathrm{d}t = \alpha\,\langle\sigma_z(t)\rangle$.

We consider three time-dependent observables: $\langle\sigma_{\parallel}\rangle \equiv \langle\sigma_z\rangle\cos\theta + \langle\sigma_x\rangle\sin\theta \equiv (\langle\boldsymbol{\sigma}\rangle\cdot\mathbf{b})$, $\langle\sigma_y\rangle$ and $\langle\sigma_{\perp}\rangle \equiv \langle\sigma_z\rangle\sin\theta - \langle\sigma_x\rangle\cos\theta \equiv (\langle\boldsymbol{\sigma}\rangle\times\mathbf{b})_y$, where the explicit $t$-dependence is omitted for brevity. Figure 6(b) shows the spiral behavior of $\langle\sigma_y\rangle$ and $\langle\sigma_{\perp}\rangle$, strongly dependent on the packet width. The radius of the spiral, decreasing with time, corresponds here to the decoherence in the spin subspace. The final stationary values depend on the width of the packet; that is, on the accuracy of the measurement. For a narrow packet, the displacement of the stationary point from the initial one is relatively small and increases in the same way as the maximum radius of the spiral, with the initial width $w$. Next, we consider asymptotic values of spin components to see the steady states, $t \to \infty$, produced by a long measurement. At long times, $C$ and $S$ defined above in equation (28) as $C \equiv \cos(t\sqrt{q^2\alpha^2 + \widetilde{\Delta}^2}/2)$ and $S \equiv \sin(t\sqrt{q^2\alpha^2 + \widetilde{\Delta}^2}/2)$, become rapidly oscillating, on the scale of the order of $1/t\alpha$, functions of momentum $q$. As a result, in calculations of integrals containing bilinear forms of these functions, one can use the semiclassical integration rule by substituting in the integrands $C^2$ and $S^2$ with $1/2$ and $CS$ with zero [47]. Then, by using equations (6) and (7), with the Green function (28)–(30), initial state (35) and definition of observables (39), we obtain $\langle\sigma_{\parallel}(\infty)\rangle$ in the form

$$\langle\sigma_{\parallel}(\infty)\rangle = w\int_{-\infty}^{\infty}\frac{\mathrm{d}q}{2\sqrt{\pi}}\mathrm{e}^{-q^2w^2/4} \times\frac{\cos\beta[q^2\cos\theta + q(\cos^2\theta+1) + \cos\theta] + \sin\beta\sin\theta\cos\phi\,(q\cos\theta+1)}{(q+\cos\theta)^2 + \sin^2\theta}. \tag{41}$$

We can study limiting cases of equation (41). The first limit is the weak spin–orbit coupling; that is, a broad initial packet, $w \gg \alpha/\widetilde{\Delta}$. Here, the range of possible momenta goes to zero, and one can substitute $q = 0$ in the fraction in the integral to obtain $\langle\sigma_{\parallel}(\infty)\rangle = \cos\theta\cos\beta + \sin\theta\cos\phi\sin\beta$. For a strong spin–orbit coupling, i.e. for a narrow packet, one can neglect powers of $q$ lower than $q^2$ and obtain $\langle\sigma_{\parallel}(\infty)\rangle = \cos\theta\cos\beta$.

The orthogonal component can be written as

$$\langle\sigma_{\perp}(\infty)\rangle = w\sin\theta\int_{-\infty}^{\infty}\frac{\mathrm{d}q}{2\sqrt{\pi}}\mathrm{e}^{-q^2w^2/4}\,\frac{\cos\beta(q^2+q\cos\theta) + q\cos\phi\sin\beta\sin\theta}{(q+\cos\theta)^2+\sin^2\theta}. \tag{42}$$

In limiting cases, as considered under equation (41), we obtain $\langle\sigma_{\perp}(\infty)\rangle = 0$ for weak spin–orbit coupling and $\langle\sigma_{\perp}(\infty)\rangle = \sin\theta\cos\beta$ for strong spin–orbit coupling. The component $\langle\sigma_y(\infty)\rangle = 0$ for any coupling strength.

It is instructive to compare the obtained asymptotic behavior with that intuitively expected in a simple case of commuting Zeeman and spin–orbit couplings; i.e. $\theta = 0$. Here, the overlap

of the functions $\Psi_1(x|t) = \psi_0(x - \alpha t)$ and $\Psi_2(x|t) = \psi_0(x + \alpha t)$ vanishes on the time scale of the order of $w/\alpha$, and the spin state becomes mixed, as can be seen in equation (40). The expectation values of spin components $\langle\sigma_z\rangle = \cos\beta$ and $\langle\sigma_y\rangle = 0$ are time-independent. The $x-$component changes from $\langle\sigma_x(0)\rangle = \sin\beta$ to $\langle\sigma_x(\infty)\rangle = 0$, in agreement with (41) and (42). The spirals in figure 6 are transformed into projection of a log connecting points $(\sin\beta, 0, \cos\beta)$ and $(0, 0, \cos\beta)$ on the Bloch sphere and inside the Bloch ball, correspondingly.

## 4. Conclusions and possible extensions

In summary, we have shown that motion in the spin–orbit coupling fields simulates a von Neumann measurement of a spin-1/2 system. The spin–orbit dynamics map spin motion onto a spin-dependent coordinate walk, thus making distinguishable otherwise hidden virtual histories of spins. The accuracy of the measurement depends on the resources available in the momentum space; that is, on the spatial width of the initial state. We considered two examples of such a procedure: simultaneous measurement of two non-commuting spin components and measurement of a spin rotating in an external magnetic field. In the first case, since the virtual Feynman paths can be divided into infinitely small pieces in the time domain, the produced angular density distribution is time-independent at any measurement duration. As a result, any attempt of instantaneous measurement of non-commuting spin components fails, and the averages of the spin components over the measurement time are observed with the accuracy determined by the width of the initial wave packet. In the second case, the average of a single spin component corresponding to the spin–orbit coupling axis for a particle moving in one dimension is measured. We showed that even if the mass of the particle is infinite, the initial packet broadens due to spin–orbit coupling, the motion in the coordinated space is complicated, the spin state becomes mixed rather than pure, and decoherence in the spin subspace occurs.

To conclude, we mention several extensions and generalizations of the von Neumann measurement procedure seen in the physics of spin–orbit coupling.

The first extension can be related to the manifestation of the Zeno effect [45]; that is, slowing down the dynamics of a constantly measured system. Recent direct calculations indeed demonstrated that in the presence of strong driving electric fields [48] or strong spin–orbit coupling [49] the dynamics of the system become much slower than expected from the linear response approach. It would be of interest to see the relation between these results and the Zeno effect.

The second extension is related to generalizations for other systems and Hamiltonians. Recent developments in producing synthetic spin–orbit coupling allows one to realize three-dimensional spin–orbit coupling [50] in the $(\mathbf{k}\cdot\boldsymbol{\sigma})$ form. Therefore, an attempt of the von Neumann measurement for all three spin components can be made in a single experiment, providing another realization of full qubit monitoring [51]. A similar problem is spin–orbit coupling in a system with $SU(3)$ symmetry, as can be realized in cold atomic gases [52]. Here, the linear in momentum Hamiltonian is expressed in terms of the eight generators of the $SU(3)$ group, rather than simply in terms of spin-1 axis projections. As a result, the problem of spin component measurements becomes more complicated than in the case of spin-1/2, where the number of $SU(2)$ group generators is the same as the number of coordinate axes.

Another example is provided by holes in two-dimensional semiconductor structures, presenting the realization [1] of the $k^3$ rather than linear in $k$ Rashba model. Although the von Neumann measurement assumes the linear coupling, a similar qualitative analysis can be performed here. Taking into account that the spin–orbit splitting here is proportional to $\gamma k^3$, where $\gamma$ is the coupling constant [9], the conditions of accurate measurement can be reformulated as $\gamma M > w$ and $\gamma T > w^3$, and, therefore, a narrow packet (small $w$) is needed for this purpose. The realization of this measurement requires a separate discussion.

## Acknowledgment

This work was supported by the University of Basque Country UPV/EHU under program UFI 11/55, Spanish MEC (FIS2012-36673-C03-01) and 'Grupos Consolidados UPV/EHU del Gobierno Vasco' (IT-472-10).

## References

[1] Winkler R 2003 *Spin–Orbit Coupling Effects in Two-Dimensional Electron and Hole Systems* (*Springer Tracts in Modern Physics*) (Berlin: Springer)
[2] Zutic I, Fabian J and Das Sarma S 2004 *Rev. Mod. Phys.* **76** 323
[3] Dyakonov M I (ed) 2008 *Spin Physics in Semiconductors* (*Springer Series in Solid-State Sciences*) (Berlin: Springer)
[4] Wu M W, Jiang J H and Weng M Q 2010 *Phys. Rep.* **493** 61
[5] Glazov M M 2012 *Phys. Solid State* **54** 1
[6] Karimov O Z, John G H, Harley R T, Lau W H, Flatte M E, Henini M and Airey R 2003 *Phys. Rev. Lett.* **91** 246601
[7] see e.g. Rokhinson L P, Larkina V, Lyanda-Geller Y B, Pfeiffer L N and West K W 2004 *Phys. Rev. Lett.* **93** 146601
Schliemann J, Loss D and Westervelt R M 2005 *Phys. Rev. Lett.* **94** 206801
[8] Bychkov Y A and Rashba E I 1984 *Sov. Phys. JETP Lett.* **39** 78
[9] Winkler R 2000 *Phys. Rev.* B **62** 4245
[10] Wang C, Gao C, Jian C-M and Zhai H 2010 *Phys. Rev. Lett.* **105** 160403
[11] Stanescu T, Anderson B and Galitski V 2008 *Phys. Rev.* A **78** 023616
[12] Lin Y-J, Jimenez-Garcia K and Spielman I B 2011 *Nature* **471** 83
[13] Wang P, Yu Z-Q, Fu Z, Miao J, Huang L, Chai S, Zhai H and Zhang J 2012 *Phys. Rev. Lett.* **109** 095301
[14] Sommer A, Ku M, Roati G and Zwierlein M W 2011 *Nature* **472** 201
[15] Cheuk L W, Sommer A T, Hadzibabic Z, Yefsah T, Bakr W S and Zwierlein M W 2012 *Phys. Rev. Lett.* **109** 095302
[16] Liu X-J, Borunda M F, Liu X and Sinova J 2009 *Phys. Rev. Lett.* **102** 046402
[17] Ozawa T and Baym G 2012 *Phys. Rev.* A **85** 013612
[18] Liu X-J, Liu Z-X and Cheng M 2013 *Phys. Rev. Lett.* **110** 076401
[19] Zhai H 2012 *Int. J. Mod. Phys.* B **26** 1230001
[20] Tokatly I V and Sherman E Ya 2013 *Phys. Rev.* A **87** 041602
[21] Natu S and Das Sarma S 2013 *Phys. Rev.* A **88** 033613
[22] Yu T and Wu M W 2013 *Phys. Rev.* A **88** 043634
[23] Hasan M Z and Kane C L 2010 *Rev. Mod. Phys.* **82** 3045
[24] Gierz I, Suzuki T, Frantzeskakis E, Pons S, Ostanin S, Ernst A, Henk J, Grioni M, Kern K and Ast C R 2009 *Phys. Rev. Lett.* **103** 046803

[25] Yaji K, Ohtsubo Y, Hatta S, Okuyama H, Miyamoto K, Okuda T, Kimura A, Namatame H, Taniguchi M and Aruga T 2010 *Nature Commun.* **1** 1016
[26] Mathias S *et al* 2010 *Phys. Rev. Lett.* **104** 066802
[27] Ibañez-Azpiroz J, Eiguren A, Sherman E Y and Bergara A 2012 *Phys. Rev. Lett.* **109** 156401
[28] Allahverdyan A E, Balian R and Nieuwenhuizen T M 2013 *Phys. Rep.* **525** 1
[29] Berman D H and Flatté M E 2010 *Phys. Rev. Lett.* **105** 157202
[30] Arthurs E and Kelly J L Jr 1965 *Bell Syst. Tech.* **44** 725
[31] She C Y and Heffner H Jr 1966 *Phys. Rev.* **152** 1103
[32] Levine R Y and Tucci R R 1989 *Found. Phys.* **19** 175
[33] Raymer M G 1994 *Am. J. Phys.* **62** 986
[34] D'Ariano G M, Lo Presti P and Sacchi M F 2002 *Phys. Lett.* A **292** 233
[35] Allahverdyan A E, Balian R and Nieuwenhuizen T M 2010 *Physica* E **42** 339
[36] Sokolovski D and Sherman E Ya 2011 *Phys. Rev.* A **84** 030101
[37] von Neumann J 1955 *Mathematical Foundation of Quantum Mechanics* (Princeton, NJ: Princeton University Press)
[38] Trotter F F 1959 *Proc. Am. Math. Soc.* **10** 545
[39] Feynman R P and Hibbs A R 1965 *Quantum Mechanics and Path Integrals* (New York: McGraw-Hill)
[40] Inglot M and Dugaev V K 2011 *J. Appl. Phys.* **109** 123709
[41] Abramowitz M and Stegun I A 1972 *Handbook of Mathematical Functions* (New York: Dover)
[42] Nadj-Perge S, Frolov S M, Bakkers E P A M and Kouwenhoven L P 2010 *Nature* **468** 1084
[43] Plaja L and Santos L 2002 *Phys. Rev.* A **65** 035602
[44] Meyrath T P, Schreck F, Hanssen J L, Chuu C S and Raizen M G 2005 *Phys. Rev.* A **71** 041604
[45] Sokolovski D 2011 *Phys. Rev.* A **84** 062117
Sokolovski D 2013 *Phys. Rev.* D **87** 076001
[46] Shankar R 2008 *Principles of Quantum Mechanics* (New York: Plenum Press)
[47] Landau L D and Lifshitz E M 1981 *Quantum Mechanics Non-Relativistic Theory* (New York: Butterworth-Heinemann)
[48] Khomitsky D V, Gulyaev L V and Sherman E Y 2012 *Phys. Rev.* B **85** 125312
[49] Li R, You J Q, Sun C P and Nori F 2013 *Phys. Rev. Lett.* **111** 086805
[50] Anderson B M, Juzeliunas G, Galitski V M and Spielman I B 2012 *Phys. Rev. Lett.* **108** 235301
[51] Ruskov R, Korotkov A N and Molmer K 2012 *Phys. Rev. Lett.* **105** 100506
[52] Barnett R, Boyd G R and Galitski V 2012 *Phys. Rev. Lett.* **109** 235308